International Journal of Mechanical Sciences 183 (2020) 105817

Contents lists available at ScienceDirect

International Journal of Mechanical Sciences

journal homepage: www.elsevier.com/locate/ijmecsci

Intensity of singular stress fields (ISSFs) in micro-bond test in comparison with ISSFs in pull-out test

Dong Chen, Nao-Aki Noda*, Rei Takaki, Yoshikazu Sano

Department of Mechanical Engineering, Kyushu Institute of Technology Sensui-Cho 1-1 Tobata-Ku, Kitakyushu-Shi, Fukuoka, Japan

ARTICLE INFO

Keywords:
Micro-bond test
Fiber pull-out
Intensity of singular stress field (ISSF)
Fiber/matrix interface
Finite element method (FEM)

ABSTRACT

Micro-bond test is often used to investigate fiber/matrix bonding behavior. In this experiment, the average shear stress is generally used as the interface strength without considering the singular stress. Therefore, in this paper, the intensity of singular stress field (ISSF) is newly analyzed at the fiber entry/exit points. The obtained ISSFs at the fiber entry point in micro-bond test are compared to the single fiber pull-out under the same fiber geometry. The results show that care should be taken for the previous micro-bond test geometry since the ISSF varies sensitively depending on the testing geometry. To control the initial fiber/matrix debonding and evaluate the bonding behavior correctly, suitable testing geometries are proposed in micro-bond testing.

1. Introduction

Wide application of fiber reinforced composites technology in various fields is based on taking advantage of the high strength and high stiffness of fibers. There are several micromechanics tests available to investigate the fiber/matrix bonding behavior. Pull-out test and micro-bond test are very popular at present. For example, Scheer et al. [1] experimentally investigated interfacial peeling of reinforcing fibers in micro-bond test focusing on the energy release rate. Zhandarov et al. [2,3] investigated the pull-out force versus displacement in pull-out test and micro-bond test. Yang et al. [4,5] experimentally studied the effect of a special surface treatment in glass fiber/epoxy composites focusing on the interfacial shear strength (IFSS). Those studies showed that the macroscopic properties of the composite can be improved by increasing the fiber/matrix debonding strength [6,7]. However, the macroscopic properties are rarely proportional to the microscopic properties. Moreover, the debonding strength varies depending on the testing method and testing conditions.

The finite element method (FEM) has been widely used for many engineering applications [8–10]. Regarding fiber reinforced composites, Stern et al. [11] developed a path independent integral formula for the computation of the intensity of the stress singularity by using FEM. Atkinson et al. [12], Povirk et al. [13], and Freund et al. [14] conducted fiber pullout simulation studies by using a circular rigid cylinder. Hann et al. [15] investigated the effect of contact angle, loading position and loading type in micro-bond test by using FEM. Ash et al. [16] investigated the effect of bead geometry and knife angle in micro-bond test via FEM. Zhang et al. [17] studied the effects of interfacial debonding and sliding on fracture characterization of unidirectional fiber-reinforced composites by using FEM. Brito-Santana et al. [18] studied the influence of the debonding between fiber and matrix in micro scale via the FEM. In this way, the FEM is widely used to analyze fiber reinforced composites [19–25]. Ahmed et al. [26–32] studied sensing, low loss and birefringent etc. by using FEM.

Fig. 1 shows a micro-bond test commonly used to investigate fiber/matrix bonding behavior. The green part represents the fiber and the grey portion represents matrix. Point E denotes the fiber entry point closer to the load and constraints; Point A denotes the fiber exit point. Notation l_b denotes the axial length of the bonded area from Point A to Point E before applying load P. Here, the dark portion means constraints. Notation l_g denotes the knife gap opening, that is, the horizontal distance from the constraint knife tip to the fiber surface assuming the symmetry on both sides. Fig. 2 shows the single fiber pull-out test treated in the previous paper [33,34] whose ISSF will be compared to Fig. 1.

The micro-bond test in Fig. 1 can be used more conveniently than the pull-out test in Fig. 2 where large matrix region should be prepared by molding during the cure procedure [2,35]. This is the reason why most of the previous experiments employed the micro-bond test instead of the pull-out test [3]. In the micro-bond test, the experimental results are strongly affected by the equipment geometries. Under the same fiber/matrix combination, the experimental results of in micro-bond test in Fig. 1 is quite different from that in pull-out test in Fig. 2. The difference can be characterized by the ISSFs controlling the fiber/matrix interface initial debonding.

In this paper, therefore, the ISSF of the micro-bond test will be analyzed at the fiber entry/exit points. Then, the results will be compared with the ISSF of the pull-out test [33,34] to clarify the difference be-

* Corresponding author.
E-mail address: noda.naoaki844@mail.kyutech.jp (N.-A. Noda).

https://doi.org/10.1016/j.ijmecsci.2020.105817
Received 17 January 2020; Received in revised form 13 May 2020; Accepted 23 May 2020
Available online 29 May 2020

Nomenclature

FEM	Finite element method
ISSF	Intensity of singular stress field
IFSS	Interfacial shear strength based on average shear stress
Point A	Fiber exit point for micro-bond test in Fig. 1
Point E	Fiber entry point for micro-bond test in Fig. 1
Point A^*	Fiber buried end for pull-out test in Fig. 2
Point E^*	Fiber entry point for pull-out test in Fig. 2
l_M	Size of the matrix for pull-out test
l_b	Fiber bonded length
l_g	Knife gap opening
D	Width of the fiber in 2D analysis, fixed as $D = 20\mu m$
P	Total pull-force on the free end of fiber
θ_C	Contact angle of matrix and fiber
r_i	Distance from Point i ($i = A, E, E^*$) along the interface
E_F	Young's modulus of fiber
E_M	Young's modulus of matrix and droplet
ν_F	Poisson's ratio of fiber
ν_M	Poisson's ratio of matrix and droplet
G_F	Shear modulus of fiber
G_M	Shear modulus of matrix and droplet
α, β	Dundurs' parameters
$\lambda, \lambda_1, \lambda_2$	Singular index
σ_x^i	Stress in the x-direction at Point i ($i = A, E, E^*$)
$\sigma_{x,FEM}^i(r_i)$	Stress distribution along r_i in FEM analysis.
K_{σ,λ_1}^i	ISSF at Point i ($i = A, E, E^*$) corresponding to λ_1
K_{σ,λ_2}^i	ISSF at Point i ($i = A, E, E^*$) corresponding to λ_2
K_σ^i	ISSF at Point i ($i = A, E, E^*$)
e_{min}	Minimum element size in FEM modelling
$\Delta\theta_C$	Change of θ_C after deformation
$u_y^i(0)$	Displacement in the y-direction at Point i
x	Distance from Point i the x-direction along the surface
$u_y^i(x)$	Displacement in the y-direction along the surface from Point i

tween the two popular testing methods. The effects of major geometries such as bond length l_b and knife gap opening l_g on the ISSFs in micro-bond test will be also clarified to establish the most suitable testing conditions. In the previous micro-bond tests, very small knife gap opening l_g was used without considering the singular stress. The final goal of this study is to clarify the fiber pull out mechanism toward designing suitable fiber reinforced composites.

2. Modelling to analyze intensity of singular stress filed (ISSF)

2.1. Modelling of micro-bond test in contrast to fiber pull-out test

Fig. 1 illustrates the modelling of the micro-bond test to calculate the ISSF. In contrast, Fig. 2 illustrates the modelling of the fiber pull-out test whose detail is indicated in the previous paper [33] and Appendix A. As shown in Fig. 1 and 2, a similar rectangular shaped fiber is assumed. A smaller rectangular shaped region is assumed for the droplet in Fig. 1in contrast to a larger rectangular shaped region for the matrix in Fig. 2. In real micro-bond test, the resin droplet is an irregular sphere shape restrained by the knife-edge. Although the contact angle in micro-bond test is usually $\theta_c = \pi/6 \sim \pi/4$ [2] in Fig. 1, in this simulation the contact angle $\theta_c = \pi/2$ is assumed to compare with the ISSFs under the pull-out test in Fig. 2. Under this assumption, the singular index is the same at Point E and Point E*. In both models in Fig. 1 and 2, perfectly bonded interface is assumed between the resin and the fiber with zero interface thickness. In other words, the material properties around the interface vary in a stepwise manner. Notations E_F, ν_F, E_M, ν_M represent

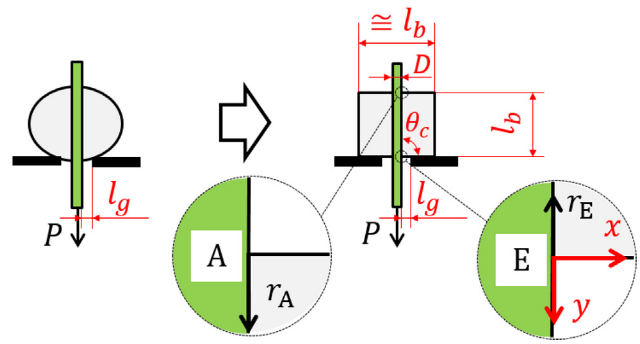

Fig. 1. Modelling of micro-bond test of a fiber with $D = 20\mu m$ and $P/D = 1$ [$N \cdot mm^{-1}$].

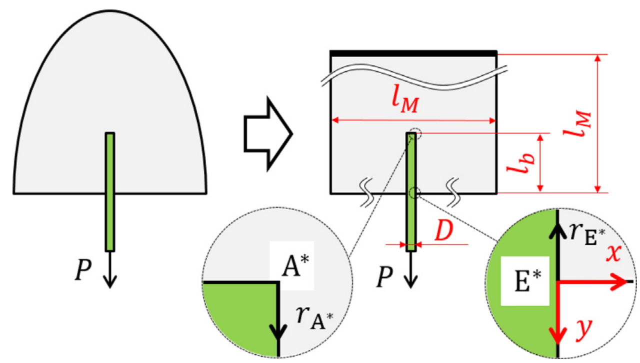

Fig. 2. Modelling of pull-out test with $D = 20\mu m$ and $P/D = 1$ [$N \cdot mm^{-1}$] [33].

the Young's modulus and Poisson's ratio of fiber and matrix, respectively. Notation D denotes the diameter of the fiber, which is the width of the fiber in the present 2D modelling. A uniform tensile stress is distributed at the end of the fiber, and the total force is P. In other words, $P/D = 1$ [$N \cdot mm^{-1}$] is normalized to analysis the ISSF. The rectangular shaped droplet is assumed as shown in Fig. 1 with the large width of the droplet in the x-direction as $l_b/2$ on each side. In other words, in this study, the 2D square shape of the droplet is assumed. Usually, the bonded area $l_b \le 250\mu m$ is used in the previous micro-bond experiments [1, 2, 6, 7, 15, 16, 36].

In this study, the ISSF in Fig. 1 is mainly discussed by varying l_b and l_g under plane strain. In the Cartesian x- and y-coordinates shown in Fig. 1 and 2, the y-direction corresponds to the axial direction of the fiber, and the x-direction corresponds to the radial direction of the fiber. Notation r_i, (i = A, E, E*), denotes the distance from Point i, (i = A, E, E*) in the y direction and $r_i = 0$ means Point i. It should be noted that shear-lag theory is widely used for considering shear stress distributions along fiber interface [37–39]. However, this theory is simply based on one dimensional assumption of the fiber and cannot express the ISSF. For example, although experiment results of the IFSS is proportional to the bonded length, the real ISSF at the entry point is not proportional to the bonded length [33, 34]. In this analysis software MSC Marc is used to analyze the micro-bond model in Fig. 1.

2.2. Singular stress field at the fiber entry/exit points

The normal singular stress, which may cause debonding at the entry point, can be expressed as follows: [40]

$$\sigma_x^i = \frac{K_{\sigma,\lambda_1}^i}{r_i^{1-\lambda_1}} + \frac{K_{\sigma,\lambda_2}^i}{r_i^{1-\lambda_2}}, \left(i = A, E, E^*\right) \quad (1)$$

Here λ_1 and λ_2 are singular indexes, which can be calculated by solving the following characteristic equations [41, 42]. Singular indexes at Point E in Fig. 1 and Point E* in Fig. 2 are same, but singular indexes

Table 1
Mechanical properties of Glass fiber/Epoxy.

	Fiber	Matrix (Droplet)
Material	Glass fiber	Epoxy
Young's Modulus (GPa)	75	3.3
Poisson's Ratio	0.17	0.35
Dundurs' Parameter	α = 0.9071	β = 0.2016
Singular Index	λ_1 = 0.6592	λ_2 = 0.9992

at Point A in Fig. 1 and Point A* in Fig. 2 are different. In micro-bond test, Point A and Point E have same singular indexes. Therefore, the ISSFs at Point A, Point E and Point E* can be compared. But they cannot be directly compared with Point A*.

$$4sin^2(\pi\lambda)\left\{sin^2\left(\frac{\pi\lambda}{2}\right)-\lambda^2\right\}\beta^2+4\lambda^2 sin^2(\pi\lambda)\alpha\beta$$
$$+\left\{sin^2\left(\frac{\pi\lambda}{2}\right)-\lambda^2\right\}\alpha^2+4\lambda^2 sin^2(\pi\lambda)\beta$$
$$+2\left\{\lambda^2\cos(2\pi\lambda)+sin^2\left(\frac{\pi\lambda}{2}\right)\cos(\pi\lambda)+\frac{1}{2}sin^2(\pi\lambda)\right\}\alpha$$
$$+sin^2\left(\frac{3\pi\lambda}{2}\right)-\lambda^2=0 \quad (2)$$

Here, α, β denote bi-material parameters of Dundurs [43], and G_F and G_M are shear modulus, which can be transformed from Young's modulus E_F, E_M and Poisson's ratios v_F, v_M. Subscripts M, F represent the matrix and the reinforcing fiber, respectively. In this study, analysis is carried out under plane strain.

$$\left.\begin{array}{l}\alpha=\frac{G_F(\kappa_M+1)-G_M(\kappa_F+1)}{G_F(\kappa_M+1)+G_M(\kappa_F+1)},\ \beta=\frac{G_F(\kappa_M-1)-G_M(\kappa_F-1)}{G_F(\kappa_M+1)+G_M(\kappa_F+1)},\\ \kappa_i=\left\{\begin{array}{l}(3-v_i)/(1+v_i)\ (Plain\ stress)\\ (3-4v_i)\ (Plain\ strain)\end{array}\right.(i=M,F)\end{array}\right\} \quad (3)$$

For the material combination as shown in Table 1, α = 0.9071, β = 0.2016, λ_1 = 0.6592, λ_2 = 0.9992. Here, λ_2 is close to 1, which means that Eq. (1) can be written as Eq. (4).

$$\sigma_x^i=\frac{K^i_{\sigma,\lambda_1}}{r_i^{1-\lambda_1}}+\frac{K^i_{\sigma,\lambda_2}}{r_i^{1-\lambda_2}}\cong\frac{K^i_{\sigma,\lambda_1}}{r_i^{1-\lambda_1}},(i=\mathrm{A,E,E^*}) \quad (4)$$

Here, K^i_{σ,λ_1} and K^i_{σ,λ_2} denote ISSFs for the normal stress at the vicinity of Point i on the interface r_i (i = A, E, E*). As the λ_2 for most material in reality is close to 1 under this geometry [44], the second term K^i_{σ,λ_2} can be omitted, ISSF K^i_σ in this study can be expressed by K^i_{σ,λ_1} corresponding with λ_1. Definition of K^i_σ are shown in Eq. (5).

$$K^i_\sigma\cong K^i_{\sigma,\lambda_1}=\lim_{r\to 0}\left[\sigma^i_x(r_i)\cdot r_i^{1-\lambda_1}\right],(i=\mathrm{A,E,E^*}) \quad (5)$$

2.3. Proportional method by using FEM

Finite element method (FEM) analysis should be well conducted and may require experience and skills for engineering applications [8–14, 17, 45]. In this analysis, a mesh independent proportional method is used to calculate the ISSF K^i_σ defined in Eq. (5). Since λ_2 is close to 1, the second term can be omitted, the ISSF can be calculated from the ratio of FEM stress $\sigma^{FEM}_{x,i}(r_i)$ as shown in Eq. (6) [40–42, 46].

$$\frac{K^i_\sigma}{K^j_\sigma}\cong\frac{\sigma^i_{x,FEM}(r_i)}{\sigma^j_{x,FEM}(r_j)},(i,j=\mathrm{A,E,E^*}) \quad (6)$$

Table 2 shows the FEM stress $\sigma^E_{x,FEM}(r_E)$ near Point E and the FEM stress ratio $\sigma^E_{x,FEM}(r_E)/\sigma^A_{x,FEM}(r_A)$. Although $\sigma^E_{x,FEM}(r_E)$ varies depending on the FEM mesh size, the FEM stress ratio $\sigma^E_{x,FEM}(r_E)/\sigma^A_{x,FEM}(r_A)$ is almost the same independent of mesh size. This is because the same mesh pattern is applied to the singular stress region to cancel the FEM error. The FEM stress ratio in Table 2 can be regarded as the real stress ratio although the FEM stress cannot express the real singular stress. Since

Table 2
FEM Stress ratio with λ^i_1 = 0.6592 when l_b = 100μm and l_g = 20μm between Point E and Point A in Fig. 1 for the material combination in Table 1.

Smallest mesh sizee_{min} = $3^{-9}D$			Smallest mesh sizee_{min} = $3^{-10}D$		
$\frac{r_i}{e_{min}}$	$\sigma^E_{x,FEM}(r_E)$[MPa]	$\frac{\sigma^E_{x,FEM}(r_E)}{\sigma^A_{x,FEM}(r_A)}$	$\frac{r_i}{e_{min}}$	$\sigma^E_{x,FEM}(r_E)$[MPa]	$\frac{\sigma^E_{x,FEM}(r_E)}{\sigma^A_{x,FEM}(r_A)}$
0.0	1.211	-1.376	0.0	1.724	-1.371
0.5	1.033	-1.371	0.5	1.469	-1.368
1.0	0.756	-1.365	1.0	1.075	-1.366
1.5	0.630	-1.359	1.5	0.896	-1.364
2.0	0.594	-1.356	2.0	0.845	-1.363

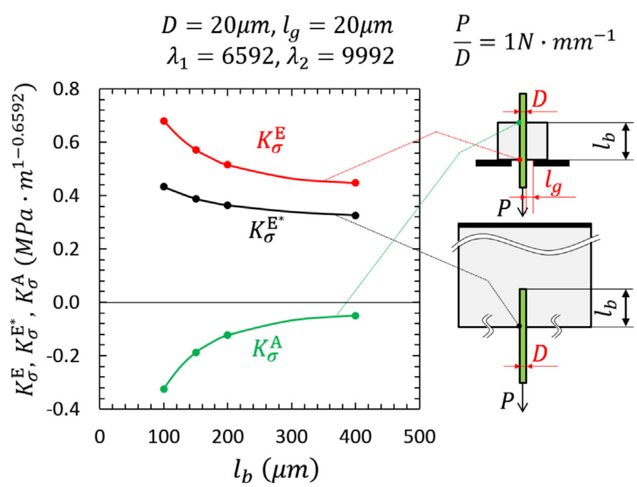

Fig. 3. ISSF variations K^A_σ, K^E_σ, $K^{E^*}_\sigma$ by varying $l_b$when l_g = 20μm in micro-bond test.

Table 3
ISSF variations K^A_σ, K^E_σ, $K^{E^*}_\sigma$ [MPa · m$^{1-0.6592}$] by varying $l_b$when l_g = 20μm in micro-bond test, (): ISSF ratio variations K^A_σ/K^E_σ and $K^{E^*}_\sigma/K^E_\sigma$ by varying l_b.

l_b[μm]	K^E_σ (K^E_σ/K^E_σ)	K^A_σ (K^A_σ/K^E_σ)	$K^{E^*}_\sigma$ ($K^{E^*}_\sigma/K^E_\sigma$)
100	0.680(1.000)	-0.324(-0.476)	0.433(0.637)
150	0.562(1.000)	-0.179(-0.318)	0.389(0.691)
200	0.515(1.000)	-0.124(-0.240)	0.364(0.707)
400	0.448(1.000)	-0.0498(-0.111)	0.326(0.728)

the stress ratio can be obtained accurately in Table 2, the ISSF can be obtained from the ISSF of reference solutions with the ratio as shown in Eq. (6). The ISSF of the pull-out test in Fig. 2 can be used as the reference solutions whose FEM modelling is indicated in the Appendix A [33,34]. In Appendix B, an example of the FEM mesh of micro-bond test is indicated in Fig. B.1. It should be noted that the FEM stress $\sigma^i_{x,FEM}(r_i)$ indicated in Table 2 is mainly controlled by the minimum element size e_{min} around the singular point.

3. Results and discussion

3.1. Bond length l_b effect on ISSF in micro-bond test

Fig. 3 and Table 3 indicate the ISSF K^E_σ at the entry point and the ISSF K^A_σ of the exit point in comparison with the ISSF $K^{E^*}_\sigma$ of the pull-out test in Fig. 2 at the entry point by varying the bond length l_b. Here, other dimensions are fixed as knife gap opening l_g = 20μm, fiber diameter D = 20μm and contact angle $\theta_C = \pi/2$ for Glass fiber/Epoxy in Table 1. Those ISSFs K^E_σ, K^A_σ, $K^{E^*}_\sigma$ decrease with increasing l_b. As shown in the interface stress distribution in Appendix B, the tensile stress appears near the entry Point E and the compressive stress appears near the exit Point A. From Fig. 3 and Table 3, no matter how the l_b changes, the entry Point E in micro-bond test is more severe for debonding.

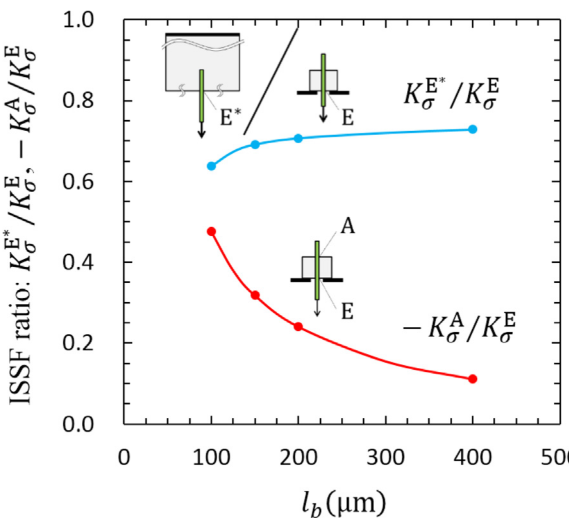

Fig. 4. ISSF ratio variations by varying l_b when $l_g = 20\mu m$.

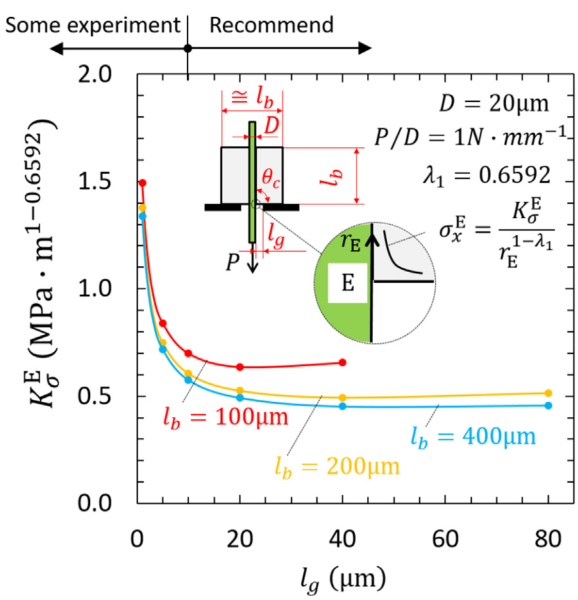

Fig. 5. ISSF variation K_σ^E by varying $l_g$when $l_b = 100\mu m$, $200\mu m$, $400\mu m$.

In the pull-out test, a similar tensile ISSF appears the entry point E* as shown in Fig. 3 and also a similar compressive ISSF appears near the end Point A* in Fig. 2. The ISSFs at Point E and Point E* decrease in a similar way by increasing l_b.

To clarify the relation between K_σ^E at Point E in micro-bond test and $K_\sigma^{E^*}$ at Point E* in pull-out test, Table 3 and Fig. 4 shows ISSF ratios $-K_\sigma^A/K_\sigma^E$ and $K_\sigma^{E^*}/K_\sigma^E$. As shown in Table 3 and Fig. 4, the ratio $-K_\sigma^A/K_\sigma^E$ decreases significantly with increasing l_b. Instead, the ratio $K_\sigma^{E^*}/K_\sigma^E$ is almost constant as $K_\sigma^{E^*}/K_\sigma^E \cong 0.75$. In other words, the ISSF at Point E in micro-bond test is about 1.5 times of that at Point E* in pull-out test. As, pull-out is relatively complex compared to the micro-bond test. The pull-out test require large size of the matrix and a complex cure procedure [2, 35]. While the micro-bond test is relatively simpler and easier compared to the pull-out test. Besides, there is more experiment study of micro-bond tests available. From the ISSF results, the micro-bond test and pull-out test are almost proportional under idealized situation. Therefore, the results of the pull-out test can be predicted by the results of micro-bond test of same material and fiber geometry.

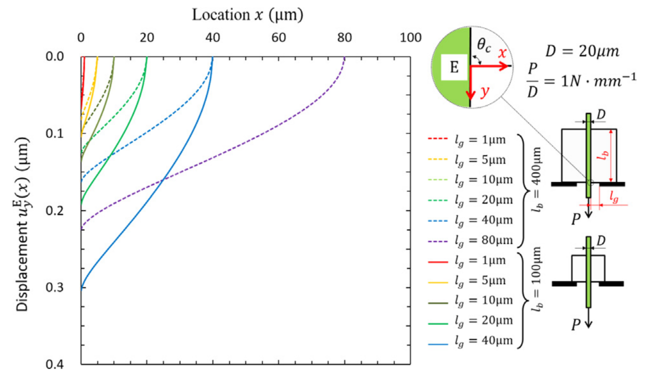

Fig. 6. Fiber deformation at the unrestrained surface by varying knife gap opening l_g for $l_b = 100\mu m$ and $l_b = 400\mu m$.

3.2. Effect of knife gap opening l_g on ISSF in micro-bond test

Table 4 and Fig. 5 illustrate the ISSF K_σ^E by varying knife gap opening l_g assuming the droplet dimensions $l_b = 100\mu m$, $200\mu m$, $400\mu m$. The result $l_b = 100\mu m$ can be shown in the range $l_g \le 40\mu m$ because larger $l_g > 40\mu m$ cannot support the smaller droplet size $l_b = 100\mu m$. In the previous experiment [1, 2, 6, 7, 15, 16, 36], the bonded length l_b, which is nearly equal to the droplet size, was in the range $l_b = 50\mu m \sim 400\mu m$ in most cases.

In Fig. 5, when $l_g \le 10\mu m$, the ISSF K_σ^E increases significantly with decreasing the knife gap opening l_g. In other words, when $l_g \le 10\mu m$, the ISSF K_σ^E is sensitive to l_g although when $l_g \ge 10\mu m$, the ISSF K_σ^E is nearly independent of l_g. When $l_b = 100\mu m$, the ISSF increases slightly with increasing l_g because of the bend deformation of the small size droplet $l_b = 100\mu m$. Since many previous tests were conducted under $l_g \le 10\mu m$ [47–49], the initial debonding condition varies depending on l_g whose slight change affects the ISSF. Therefore, as a conclusion, the micro-bond testing geometry $l_g \ge 10\mu m$ is recommended since the ISSF K_σ^E becomes almost constant as shown in Fig. 5. In the experiments, no droplet fracture should be confirmed instead of the interface debonding since the sphered droplet shape is deformed due to the knife edge support.

3.3. Resin deformation and fiber elongation in micro-bond test

To understand the geometrical effect in micro-bond test, the matrix surface deformation is studied in this section. Fig. 6 illustrates the displacement $u_y^E(x)$ when $P = 1MPa \times 0.02mm \times 1mm = 0.02N$, $l_b = 100\mu m$ and $l_b = 400\mu m$ using the cartesian coordinate system in Fig. 6 where the x-axis is the distance from Point E ($x = 0$) until the knife edge ($x = l_g$). At the knife edge $x \ge l_g$, the displacement in the y-direction is constrained with no shear stress as $u_y = 0$, $\tau_{xy} = 0$. The deformation when $l_b = 400\mu m$ is relatively smaller than the deformation when $l_b = 100\mu m$.

Table 5a, b shows displacement $u_y^E(0)$ at the entry Point E, displacement $u_y^A(0)$ at the exit Point A, and fiber elongation $u_y^E(0) - u_y^A(0)$. Table 5a, b also shows the contact angle change defined as $\Delta\theta_C = tan^{-1}[du_y^E(0)/dx]$ at Point E. Fig. 7 shows $u_y^E(0)$ and $u_y^A(0)$ both of which increase with increasing l_g although Table 5a, b shows K_σ^E decreases with increasing l_g. Since the ratio $u_y^E(0)/K_\sigma^E$ is not constant as shown in Table 5a, b, $u_y^E(0)$ is not controlled by the ISSF K_σ^E. Instead, as shown in Table 5a, b and Fig. 8, the ratio $K_\sigma^E/\Delta\theta_C$ is almost constant, and therefore, K_σ^E is almost controlled by $\Delta\theta_C$.

The reason why the ISSF K_σ^E becomes larger as $l_g \to 0$ in Fig. 5 can be explained from the surface angle after deformation defined as $\Delta\theta_C = tan^{-1}[\frac{du_y^E(0)}{dx}]$. When the knife edge gap $l_g \to 0$ in micro-bond test, the surface angle after deformation $\Delta\theta_C = tan^{-1}[\frac{du_y^E(0)}{dx}]$ becomes larger as

Table 4
ISSF variation K_σ^E $[MPa{\cdot}m^{1-0.6592}]$ by varying l_g. (): $K_\sigma^E|_{l_b}/K_\sigma^E|_{l_b=100\mu m}$.

l_b [μm]\\l_g [μm]	1	5	10	20	40	80
100	1.492(1.000)	0.840(1.000)	0.700(1.000)	0.637(1.000)	0.656(1.000)	–(–)
200	1.377(0.923)	0.749(0.891)	0.606(0.866)	0.526(0.826)	0.494(0.753)	0.515(–)
400	1.337(0.896)	0.718(0.855)	0.576(0.822)	0.493(0.773)	0.452(0.689)	0.457(–)

Table 5a
Fiber deformation when $l_b = 100\mu$m.

Knife gap opening l_g (μm)	1	5	10	20	40	80
K_σ^E	1.492	0.840	0.700	0.637	0.656	–
Displacement $u_y^E(0)$ (μm)	0.0675	0.1041	0.1362	0.1919	0.3042	–
Displacement $u_y^A(0)$ (μm)	0.0593	0.0908	0.1201	0.1729	0.2831	–
Fiber elongation $\Delta l_b = u_y^E - u_y^A$	0.0082	0.0133	0.0161	0.0190	0.0211	–
θ_C after deformation	67.1°	76.7°	78.8°	79.8°	79.5°	–
$\Delta\theta_C = tan^{-1}[\frac{du_y^E(0)}{dx}]$	22.9°	13.3°	11.2°	10.2°	10.5°	–
$u_y^E(0)/K_\sigma^E$	0.0452	0.1240	0.1945	0.3013	0.4636	–
$K_\sigma^E/\Delta\theta_C$	0.0652	0.0632	0.0625	0.0625	0.0625	–

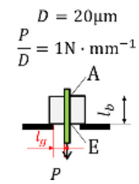

Table 5b
Fiber deformation when $l_b = 400\mu$m.

Knife gap opening l_g (μm)	1	5	10	20	40	80
K_σ^E	1.337	0.718	0.576	0.493	0.452	0.457
Displacement $u_y^E(0)$ (μm)	0.0575	0.0821	0.1004	0.1254	0.1628	0.2241
Displacement $u_y^A(0)$ (μm)	0.0349	0.0495	0.0611	0.0781	0.1058	0.1566
Fiber elongation $\Delta l_b = u_y^E - u_y^A$	0.0226	0.0326	0.0393	0.0473	0.0570	0.0675
θ_C after deformation	70.2°	79.2°	81.4°	82.8°	83.5°	83.8°
$\Delta\theta_C = tan^{-1}[\frac{du_y^E(0)}{dx}]$	19.8°	10.8°	8.6°	7.2°	6.5°	6.2°
$u_y^E(0)/K_\sigma^E$	0.0430	0.1144	0.1744	0.2545	0.3598	0.4906
$K_\sigma^E/\Delta\theta_C$	0.0674	0.0667	0.0672	0.0682	0.0700	0.0740

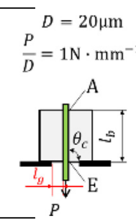

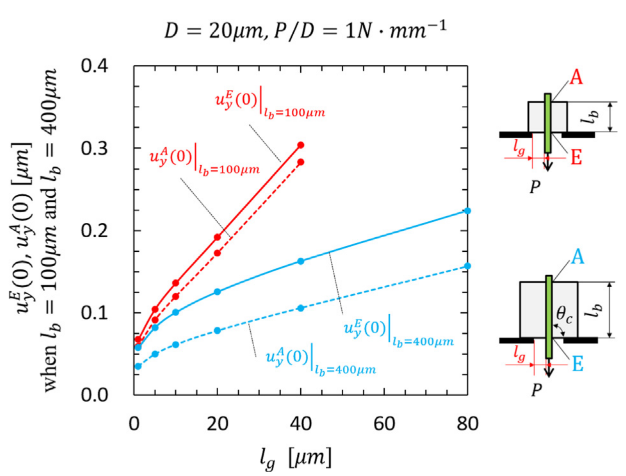

Fig. 7. Surface displacement $u_y^E(0)$ and $u_y^A(0)$ by varying knife gap opening l_g when $l_b = 100\mu m$ and $l_b = 400\mu m$.

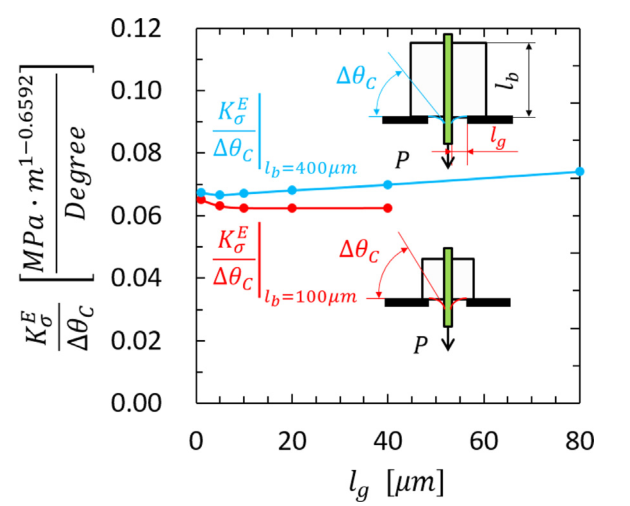

Fig. 8. ISSF ratio $K_\sigma^E/\Delta\theta_C$ is almost constant independent of l_g.

shown in Table 5a, b and Fig. 6. This is because the fiber is pulled-out under the small knife gap opening $l_g \to 0$ (see Fig. 6, for example, when $l_g = 1\mu$m). Some previous experimental studies suggested that the knife edge gap l_g should be as small as possible [47–49]. To obtain the general results independent of l_g, however, a certain gap should be kept in micro-bond test in Fig. 1.

3.4. Effect of knife edge friction on ISSF in micro-bond test

In the above discussion, no friction condition $\mu = 0$ is assumed by applying $u_y = 0$, $\tau_{xy} = 0$ along the knife edge shown in black in Fig. 1. In real micro-bond test, however, the knife edge restrains the y-displacement as $u_y = 0$ with a certain frictional stress as $\tau_{xy} \neq 0$. Since the friction coefficient μ is unknown, in this section, along the knife edge, assume another condition $u_y = 0$, $u_x = 0$, which is corresponding to $\mu \to \infty$ along the knife edge. Fig. 9 compares the two different boundary conditions under the fixed dimensions $D = 20\mu$m and $l_b = 400\mu$m. The solid line represents the ISSF K_σ^E when the droplet is supported as $u_y = 0$, $\tau_{xy} = 0$ by the knife edge. And the dashed line represents the ISSF K_σ^E when the droplet is supported as $u_y = 0$, $u_x = 0$. The ISSF of real experiment with friction can be plotted between those two lines expressing extreme cases. Since the ISSF K_σ^E under $u_y = 0$, $\tau_{xy} = 0$ is the most severe, this boundary condition is adopted in this study.

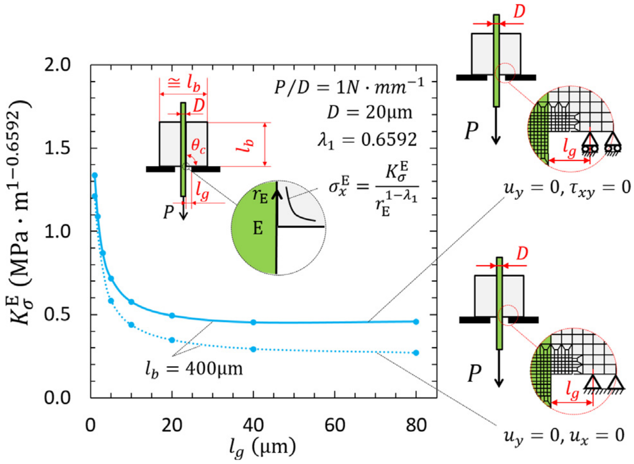

Fig. 9. Effect of friction on the knife edge on the ISSF in micro-bond test by comparing $\mu = 0$ ($u_y = 0$, $\tau_{xy} = 0$) and $\rightarrow \infty$ ($u_y = 0$, $u_x = 0$).

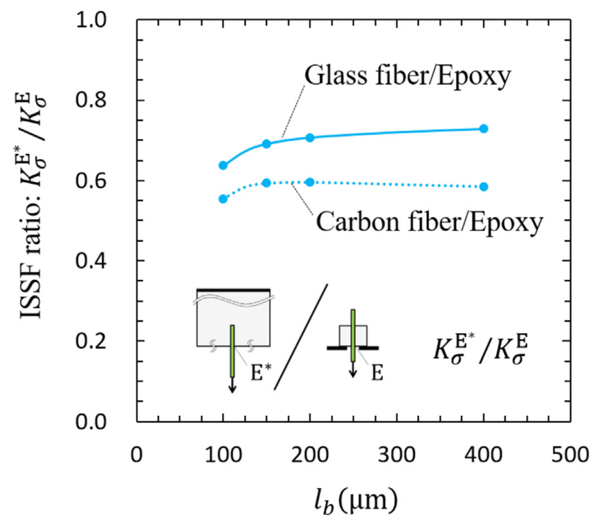

Fig. 11. ISSF ratio $K_\sigma^{E^*}/K_\sigma^E$ of pull-out test and micro-bond test when $l_g = 20\mu m$.

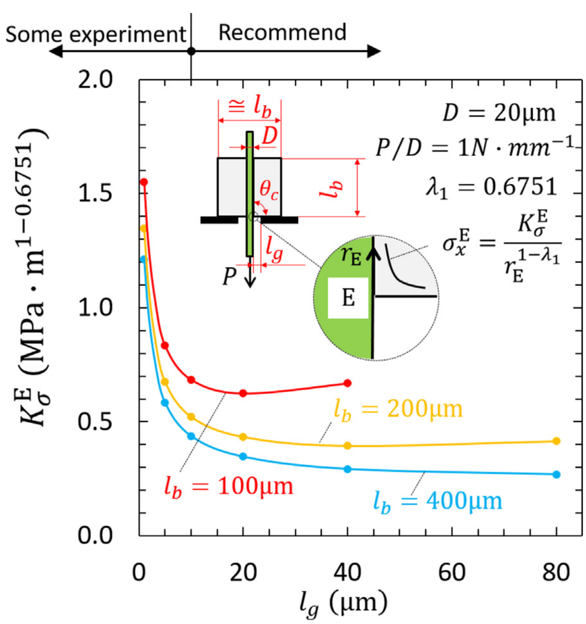

Fig. 10. ISSF K_σ^E variation by varying l_g for Carbon fiber/Epoxy.

Table 8
ISSF K_σ^E in micro-bond test when $l_g = 20\mu m$ and $K_\sigma^{E^*}$ in pull-out test of Carbon fiber/Epoxy.

l_b [μm]	100	150	200	400
$K_\sigma^{E^*}$ [$MPa \cdot m^{1-0.6751}$]	0.346	0.291	0.259	0.203
K_σ^E [$MPa \cdot m^{1-0.6751}$]	0.624	0.491	0.434	0.347
$K_\sigma^{E^*}/K_\sigma^E$	0.554	0.593	0.596	0.585

Table 6
Mechanical properties of Carbon fiber/Epoxy.

	Fiber	Matrix (Droplet)
Material	Carbon fiber	Epoxy
Young's Modulus (GPa)	276	3.03
Poisson's Ratio	0.30	0.35
Dundurs' Parameter	$\alpha = 0.9775\beta = 0.2250$	
Singular Index	$\lambda_1 = 0.6751\lambda_2 = 0.9999$	

3.5. ISSF in micro-bond test for carbon fiber/epoxy in comparison with glass fiber/epoxy

In Section 3.2, for the glass fiber/epoxy in Table 1, the effect of knife gap opening l_g on the ISSF K_σ^E was discussed as shown in Table 4 and Fig. 5. Then, it was found that when $l_g \leq 10\mu m$ commonly used, the ISSF K_σ^E is very sensitive to l_g. As a conclusion, $l_g \geq 10\mu m$ is recommended for suitable testing geometry since the ISSF K_σ^E becomes almost constant. To verify this conclusion, for carbon fiber/epoxy in Table 6, the effect of knife gap opening l_g on the ISSF K_σ^E was discussed as shown in Table 7 and Fig. 10. Here, the singular index for Carbon fiber/Epoxy at Point E is $\lambda_{1,C} = 0.6751$ instead of the singular index for Glass fiber/Epoxy $\lambda_{1,g} = 0.6592$. Table 7 and Fig. 10 illustrate the ISSF K_σ^E by varying knife gap opening l_g when the droplet dimensions $l_b = 100\mu m$, $200\mu m$, $400\mu m$ in a similar way of Table 4 and Fig. 5. The effect of l_g on the ISSF results in Fig. 10 is similar to Fig. 5 since the ISSF K_σ^E is sensitive to l_g when $l_g \leq 10\mu m$ and almost independent of l_g when $\geq 10\mu m$. Therefore, to improve the accuracy of micro-bond test, a certain gap l_g should be kept.

As shown in Table 3 and Fig. 4 in Section 3.1, for Glass fiber/Epoxy, the ISSF ratio $K_\sigma^{E^*}/K_\sigma^E$ is almost constant as $K_\sigma^{E^*}/K_\sigma^E \cong 0.75$. In other words, the ISSF at Point E in micro-bond test is about 1.5 times of that at Point E* in pull-out test. In this section, for Carbon fiber/Epoxy in Table 6, the ISSF ratio $K_\sigma^{E^*}/K_\sigma^E$ is investigated. Table 8 and Fig. 11 show the ISSF ratio $K_\sigma^{E^*}/K_\sigma^E \cong 0.60$ for Carbon fiber/Epoxy. In other words, the ISSF at Point E in micro-bond test is about 1.66 times of that at Point E* in pull-out test. In Fig. 11, both ISSF ratios are nearly constant

Table 7
ISSF variation K_σ^E [MPa · m$^{1-0.6751}$] by varying l_g for Carbon fiber/Epoxy. (): $K_\sigma^E|_{l_b}/K_\sigma^E|_{l_b=100\mu m}$.

l_b [μm]\\l_g [μm]	1	5	10	20	40	80
100	1.552(1.000)	0.834(1.000)	0.685(1.000)	0.624(1.000)	0.669(1.000)	–(–)
200	1.346(0.867)	0.675(0.809)	0.523(0.763)	0.434(0.696)	0.395(0.591)	0.415(–)
400	1.213(0.782)	0.583(0.699)	0.437(0.638)	0.347(0.556)	0.293(0.438)	0.269(–)

independent of $l_b$as $K_\sigma^{E^*}/K_\sigma^{E} \cong 0.60 \sim 0.75 \cong 0.66$. The ISSF of pull-out test can be roughly estimated from the ISSF of micro-bond test.

4. Conclusions

Micro-bond test has been used to investigate fiber/matrix bonding behavior without considering the singular stress. This paper newly analyzed the intensity of singular stress field (ISSF) at the fiber entry point under tension and the ISSF at the fiber exit point under compression. The results showed that no matter how the fiber bond length l_b changes, the fiber entry point is more dangerous in micro-bond test. Instead, in a fiber pull-out test, the fiber end point can be more dangerous if the embedded length is shorter. The ISSF at the entry point in micro-bond test is about 1.5 times of the ISSF of pull-out test at the entry point under the same geometries D and l_b. By using this knowledge, the ISSFs of pull-out test can be predicted from micro-bond test. Care should be taken for the small knife gap opening $l_g \leq 10\mu$m popularly used in micro-bond testing because the ISSF K_σ^E is sensitive to l_g. Instead, testing geometry $l_g \geq 10\mu$m can be recommended since the ISSF K_σ^E is nearly independent of l_g.

CRediT authorship contribution statement

Dong Chen: Formal analysis, Software, Data curation. **Nao-Aki Noda:** Methodology, Conceptualization, Supervision. **Rei Takaki:** Resources, Data curation. **Yoshikazu Sano:** Conceptualization.

Declaration of Competing Interests

The authors declare that they have no known competing financial interests or personal relationships that could have appeared to influence the work reported in this paper.

Appendix A. Modelling of a single fiber pull-out embedded in a semi-infinite region

Fig. 2 shows the pull-out test of a single fiber partially embedded in a semi-infinite resin matrix region studied in the previous paper [33, 34]. Here, Point A* denotes the fiber end, and Point E* denotes the fiber/surface entry point. Notation l_b denotes the axial bonded length from the end Point A* to the entry Point E* before applying load P. Notation l_M denote the size of the matrix. ISSF at Point A* and Point E* in pull-out model were discussed. Point E* is more severe than Point A*, if l_b is large enough. A two-dimensional rectangular shaped fiber was considered in the matrix whose size l_M in Fig. 2 is set as $l_M = 4000D$ [33]. Table A.1 shows the stress $\sigma_{x,FEM}^{E^*}(r_{E^*})$ near Point E* in Fig. 2 by varying

Table A.1
FEM Stress $\sigma_{x,FEM}^{E^*}(r_{E^*})$ [MPa] in Fig. 2.

l_M	2000D	4000D	6000D
r_{E^*}/e_{min} =0.0	0.763	0.771	0.771
r_{E^*}/e_{min} = 0.5	0.651	0.658	0.658
r_{E^*}/e_{min} = 1.0	0.477	0.482	0.482
r_{E^*}/e_{min} = 1.5	0.397	0.401	0.401
r_{E^*}/e_{min} = 2.0	0.374	0.378	0.378

the matrix size l_M. It is seen that $l_M = 4000D$ is large enough to express the semi-infinite region since the stress $\sigma_{x,FEM}^{E^*}(r_{E^*})$ is the same when $l_M \geq 4000D$.

Appendix B. An example of FEM mesh and stress distributions for the micro-bond test

Fig. B.1 shows an example of FEM mesh. Smaller mesh is applied at the interface corner. The minimum element size $e_{min} = 3^{-9}D$ and $e_{min} = 3^{-10}D$ are chosen confirming the mesh independency. To represent the knife edge support in Fig. 1, the y-direction displacement is fixed with no shear stress as shown in Fig. B.1. The distance from the knife edge to the fiber surface is denoted by l_g.

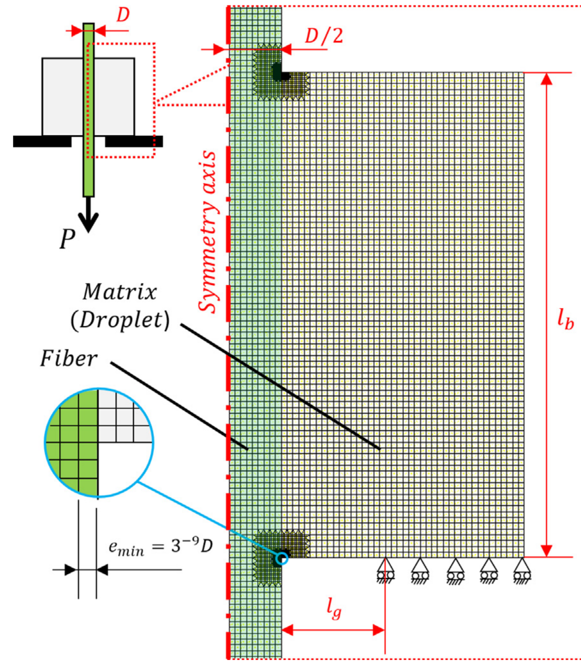

Fig. B.1. An example of FEM mesh whose minimum element size $e_{min} = 3^{-9}D$.

Fig. B.2 shows the FEM stress $\sigma_{x,FEM}$ distribution when $e_{min} = 3^{-9}D$, $l_b = 100\mu$m and $l_g = 20\mu$m focusing on Point E and Point A. The stress $\sigma_{x,FEM}$ around Point E is under tension and the stress $\sigma_{x,FEM}$ around Point A is under compression. Fig. B.3 shows the stress $\sigma_{x,FEM}(y)$ and the shear stress $\tau_{yx,FEM}(y)$ along the entire fiber/droplet interface. Here, the y-coordinate indicates the location from Point A at $y = 0$ to Point E at $y = 100\mu$m. Since the stress at the vicinity of Point A and Point E goes to infinity, minimum element size $e_{min} = 3^{-9}D$ is used around the singular points in Fig. B.1.

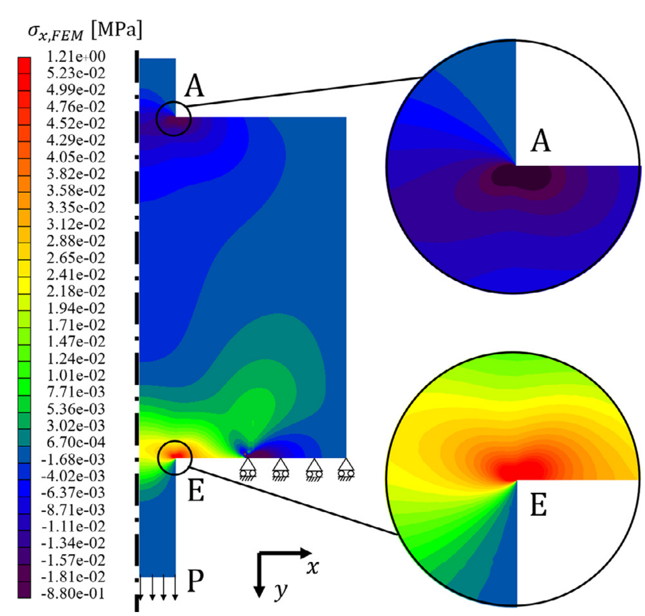

Fig. B.2. FEM stress $\sigma_{x,FEM}^{A,E}$ when $e_{min} = 3^{-9}D$, $l_b = 100\mu$m and $l_g = 20\mu$m.

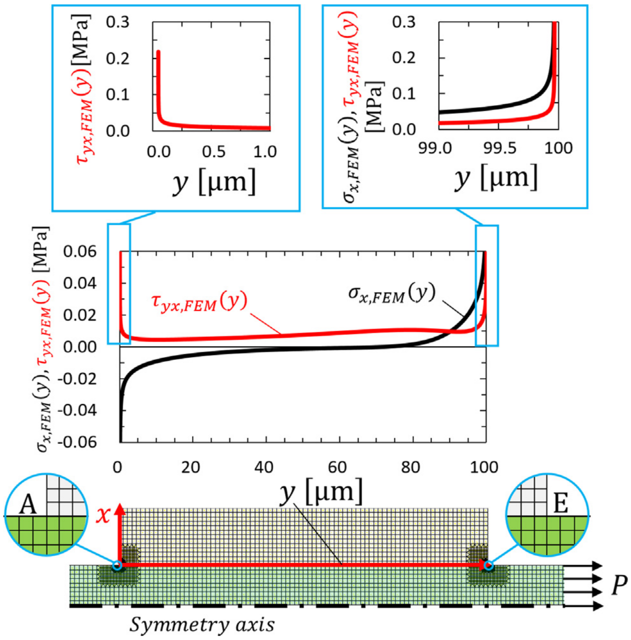

Fig. B.3. FEM stress $\sigma^{A,E}_{x,FEM}$ and $\tau^{A,E}_{xy,FEM}$ when $e_{min} = 3^{-9}D$, $l_b = 100\mu$m and $l_g = 20\mu$m along the entire fiber/matrix interface.

References

[1] Scheer RJ, Nairn JA. A comparison of several fracture mechanics methods for measuring interfacial toughness with microbond tests. J Adhes 1995;53:45–68. https://doi.org/10.1080/00218469508014371.

[2] Pisanova E, Zhandarov S, Mäder E, Ahmad I, Young RJ. Three techniques of interfacial bond strength estimation from direct observation of crack initiation and propagation in polymer-fibre systems. Compos Part A Appl Sci Manuf 2001;32:435–43. https://doi.org/10.1016/S1359-835X(00)00054-3.

[3] Zhandarov S, Mäder E. Characterization of fiber/matrix interface strength: Applicability of different tests, approaches and parameters. Compos Sci Technol 2005;65:149–60. https://doi.org/10.1016/j.compscitech.2004.07.003.

[4] Yang B, Xuan F-Z, Lei H, Wang Z, Xiang Y, Yang K, et al. Simultaneously enhancing the IFSS and monitoring the interfacial stress state of GF/epoxy composites via building in the MWCNT interface sensor. Compos Part A Appl Sci Manuf 2018;112:161–7. https://doi.org/10.1016/j.compositesa.2018.06.006.

[5] Yang B, Xuan F-Z, Wang Z, Chen L, Lei H, Liang W, et al. Multi-functional interface sensor with targeted IFSS enhancing, interface monitoring and self-healing of GF/EVA thermoplastic composites. Compos Sci Technol 2018;167:86–95. https://doi.org/10.1016/j.compscitech.2018.07.037.

[6] Baley C, Grohens Y, Busnel F, Davies P. Application of interlaminar tests to marine composites. relation between glass fibre/polymer interfaces and interlaminar properties of marine composites. Appl Compos Mater 2004;11:77–98. https://doi.org/10.1023/B:ACMA.0000012884.02847.65.

[7] Miller B, Muri P, Rebenfeld L. A microbond method for determination of the shear strength of a fiber/resin interface. Compos Sci Technol 1987;28:17–32. https://doi.org/10.1016/0266-3538(87)90059-5.

[8] Noda N-A, Chen X, Sano Y, Wahab MA, Maruyama H, Fujisawa R, et al. Effect of pitch difference between the bolt-nut connections upon the anti-loosening performance and fatigue life. Mater Des 2016;96:476–89. https://doi.org/10.1016/j.matdes.2016.01.128.

[9] Noda N-A, Takaki R, Shen Y, Inoue A, Sano Y, Akagi D, et al. Strain rate concentration factor for flat notched specimen to predict impact strength for polymeric materials. Mech Mater 2019;131:141–57. https://doi.org/10.1016/j.mechmat.2019.01.011.

[10] Wang Z, Noda N-A, Ueno M, Sano Y. Optimum design of ceramic spray coating evaluated in terms of intensity of singular stress field. Steel Res Int 2017;88. https://doi.org/10.1002/srin.201600353.

[11] Stern M, Soni ML. On the computation of stress intensities at fixed-free corners. Int J Solids Struct 1976;12:331–7. https://doi.org/10.1016/0020-7683(76)90023-8.

[12] Atkinson C, Avila J, Betz E, Smelser RE. The rod pull out problem, theory and experiment. J Mech Phys Solids 1982;30:97–120. https://doi.org/10.1016/0022-5096(82)90019-9.

[13] Povirk GL, Needleman A. Finite element simulations of fiber pull-out. J Eng Mater Technol Trans ASME 1993;115:286–91. https://doi.org/10.1115/1.2904220.

[14] Freund LB. Axial force needed to slide a circular fiber along a hole in an elastic material and implications for fiber pull-out. Eur J Mech A/Solids 1992;11:1–19.

[15] Hann LP, Hirt DE. Simulating the microbond technique with macrodroplets. Compos Sci Technol 1995;54:423–30. https://doi.org/10.1016/0266-3538(95)00080-1.

[16] Ash JT, Cross WM, Svalstad D, Kellar JJ, Kjerengtroen L. Finite element evaluation of the microbond test: meniscus effect, interphase region, and vise angle. Compos Sci Technol 2003;63:641–51. https://doi.org/10.1016/S0266-3538(02)00256-7.

[17] Zhang X, Liu H-Y, Mai Y-W. Effects of fibre debonding and sliding on the fracture behaviour of fibre-reinforced composites. Compos Part A Appl Sci Manuf 2004;35:313–23. https://doi.org/10.1016/j.compositesa.2004.03.011.

[18] Brito-Santana H, Thiesen JLM, de Medeiros R, Ferreira AJM, Rodríguez-Ramos R, Tita V. Multiscale analysis for predicting the constitutive tensor effective coefficients of layered composites with micro and macro failures. Appl Math Model 2019;75:250–66. https://doi.org/10.1016/j.apm.2019.05.031.

[19] Ranjbarian M, Mechtcherine V, Zhang Z, Curosu I, Storm J, Kaliske M. Locking Front Model for pull-out behaviour of PVA microfibre embedded in cementitious matrix. Cem Concr Compos 2019;103:318–30. https://doi.org/10.1016/j.cemconcomp.2019.04.031.

[20] Storm J, Ranjbarian M, Mechtcherine V, Scheffler C, Kaliske M. Modelling of fibre-reinforced composites via fibre super-elements. Theor Appl Fract Mech 2019;103. https://doi.org/10.1016/j.tafmec.2019.102294.

[21] Vázquez-Rodríguez JM, Flores-Johnson EA, Herrera-Franco PJ, Gonzalez-Chi PI. Photoelastic and numerical analyses of the stress distribution around a fiber in a pull-out test for a thermoplastic fiber/epoxy resin composite. Polym Compos 2018;39:E2397–406. https://doi.org/10.1002/pc.24709.

[22] Frikha M, Nouri H, Guessasma S, Roger F, Bradai C. Interfacial behaviour from pull-out tests of steel and aluminium fibres in unsaturated polyester matrix. J Mater Sci 2017;52:13829–40. https://doi.org/10.1007/s10853-017-1486-7.

[23] Serra J, Bouvet C, Castanié B, Petiot C. Experimental and numerical analysis of carbon fiber reinforced polymer notched coupons under tensile loading. Compos Struct 2017;181:145–57. https://doi.org/10.1016/j.compstruct.2017.08.090.

[24] Poniznik Z, Nowak Z, Basista M. Numerical modeling of deformation and fracture of reinforcing fibers in ceramic-metal composites. Int J Damage Mech 2017;26:711–34. https://doi.org/10.1177/1056789515611945.

[25] Kundalwal SI, Kumar S. Multiscale modeling of stress transfer in continuous microscale fiber reinforced composites with nano-engineered interphase. Mech Mater 2016;102:117–31. https://doi.org/10.1016/j.mechmat.2016.09.002.

[26] Paul BK, Ahmed K, Vigneswaran D, Ahmed F, Roy S, Abbott D. Quasi-photonic crystal fiber-based spectroscopic chemical sensor in the terahertz spectrum: design and analysis. IEEE Sens J 2018;18:9948–54. https://doi.org/10.1109/JSEN.2018.2872892.

[27] Jabin MA, Ahmed K, Rana MJ, Paul BK, Islam M, Vigneswaran D, et al. Surface plasmon resonance based titanium coated biosensor for cancer cell detection. IEEE Photonics J 2019;11. https://doi.org/10.1109/JPHOT.2019.2924825.

[28] Ahmed K, Haque MJ, Jabin MA, Paul BK, Amiri IS, Yupapin P. Tetra-core surface plasmon resonance based biosensor for alcohol sensing. Phys B Condens Matter 2019;570:48–52. https://doi.org/10.1016/j.physb.2019.05.047.

[29] Ahmed K, Paul BK, Jabin MA, Biswas B. FEM analysis of birefringence, dispersion and nonlinearity of graphene coated photonic crystal fiber. Ceram Int 2019;45:15343–7. https://doi.org/10.1016/j.ceramint.2019.05.027.

[30] Paul BK, Chakma S, Khalek MA, Ahmed K. Silicon nano crystal filled ellipse core based quasi photonic crystal fiber with birefringence and very high nonlinearity. Chinese J Phys 2018;56:2782–8. https://doi.org/10.1016/j.cjph.2018.09.030.

[31] Thenmozhi H, Mani Rajan MS, Ahmed K. D-shaped PCF sensor based on SPR for the detection of carcinogenic agents in food and cosmetics. Optik (Stuttg) 2019;180:264–70. https://doi.org/10.1016/j.ijleo.2018.11.098.

[32] Ahmed K, Paul BK, Vasudevan B, Rashed ANZ, Maheswar R, Amiri IS, et al. Design of D-shaped elliptical core photonic crystal fiber for blood plasma cell sensing application. Results Phys 2019;12:2021–5. https://doi.org/10.1016/j.rinp.2019.02.026.

[33] Noda N-A, Chen D, Zhang G, Sano Y. Single-fiber pull-out analysis comparing the intensities of singular stress fields (ISSFs) at fiber end / entry points. Int J Mech Sci 2020;165:105196. https://doi.org/10.1016/j.ijmecsci.2019.105196.

[34] Noda N-A, Chen D, Takaki R, Inoue A, Zhang G, Sano Y. Intensity of singular stress fields of an embedded fiber under pull-out force. Zair Soc Mater Sci Japan 2018;67:1073–9. https://doi.org/10.2472/jsms.67.1073.

[35] Tsai K-H, Kim K-S. The micromechanics of fiber pull-out. J Mech Phys Solids 1996;44:1147–59. https://doi.org/10.1016/0022-5096(96)00019-1.

[36] Gao S-L, Mäder E, Zhandarov SF. Carbon fibers and composites with epoxy resins: topography, fractography and interphases. Carbon N Y 2004;42:515–29. https://doi.org/10.1016/j.carbon.2003.12.085.

[37] Goda K. Semi-discretization analysis for the shear-lag model with a viscoelastic matrix and its application to creep-rupture simulation using the bis method. Nihon Kikai Gakkai Ronbunshu. A Hen/Trans Japan Soc Mech Eng Part A 2000;66:480–8. https://doi.org/10.1299/kikaia.66.480.

[38] Hedgepeth JM, Van Dyke P. Local stress concentrations in imperfect filamentary composite materials. J Compos Mater 1967;1:294–309. https://doi.org/10.1177/002199836700100305.

[39] Batdorf SB. Note on shear interaction between two fibers. Eng Fract Mech 1983;18:1207–10. https://doi.org/10.1016/0013-7944(83)90014-0.

[40] Miyazaki T, Noda N-A, Sano Y. A precise and efficient analytical method to obtain two distinct intensities of singular stress fields for single lap joint. J Japan Inst Electron Packag 2018;21:166–77. https://doi.org/10.5104/jiep.21.166.

[41] Bogy DB. Edge-bonded dissimilar orthogonal elastic wedges under normal and shear loading. J Appl Mech Trans ASME 1964;35:460–6. https://doi.org/10.1115/1.3601236.

[42] Bogy DB. Two edge-bonded elastic wedges of different materials and wedge angles under surface tractions. J Appl Mech Trans ASME 1971;38:377–86. https://doi.org/10.1115/1.3408786.

[43] Dundurs J. Effect of elastic constants on stress in a composite under plane deformation. J Compos Mater 1967;1:310–22. https://doi.org/10.1177/002199836700100306.

[44] Li R, Noda N-A, Takaki R, Sano Y, Takase Y, Miyazaki T. Most suitable evaluation method for adhesive strength to minimize bend effect in lap joints in terms of the intensity of singular stress field. Int J Adhes Adhes 2018;86:45–58. https://doi.org/10.1016/j.ijadhadh.2018.08.006.

[45] Hutchinson JW, Jensen HM. Models of fiber debonding and pull-out in brittle composites with friction. Mech Mater 1990;9:139–63. https://doi.org/10.1016/0167-6636(90)90037-G.

[46] Oda K, Kamisugi K, Noda N-A. Analysis of stress intensity factor for interface cracks based on proportional method. Nihon Kikai Gakkai Ronbunshu. A Hen/Trans Japan Soc Mech Eng Part A 2009;75:476–82. https://doi.org/10.1299/kikaia.75.476.

[47] Chou CT, Gaur U, Miller B. The effect of microvise gap width on microbond pull-out test results. Compos Sci Technol 1994;51:111–16. https://doi.org/10.1016/0266-3538(94)90161-9.

[48] Latour RA, Black J, Miller B. Fracture mechanisms of the fiber/matrix interfacial bond in fiber-reinforced polymer composites. Surf Interface Anal 1991;17:477–84. https://doi.org/10.1002/sia.740170711.

[49] Rao V, Herrera-Franco P, Ozzello AD, Drzal LT. A direct comparison of the fragmentation test and the microbond pull-out test for determining the interfacial shear strength. J Adhes 1991;34:65–77. https://doi.org/10.1080/00218469108026506.